The Astrophysical Journal, 779:126 (12pp), 2013 December 20 doi:10.1088/0004-637X/779/2/126

MULTI-WAVELENGTH MODELING OF GLOBULAR CLUSTERS—THE MILLISECOND PULSAR SCENARIO

A. Kopp[1], C. Venter, I. Büsching, and O. C. de Jager[2]
Centre for Space Research, North-West University, Potchefstroom Campus, Private Bag X6001, Potchefstroom 2520, South Africa
Received 2013 May 4; accepted 2013 October 30; published 2013 December 2

ABSTRACT

The potentially large number of millisecond pulsars (MSPs) in globular cluster (GC) cores makes these parent objects ideal laboratories for studying the collective properties of an ensemble of MSPs. Such a population is expected to radiate several spectral components in the radio through γ-ray waveband. First, pulsed emission is expected via curvature and synchrotron radiation (CR and SR) and possibly even via inverse Compton (IC) scattering inside the pulsar magnetospheres. Second, unpulsed emission should transpire through the continuous injection of relativistic leptons by the MSPs into the ambient region, which in turn produce SR and IC emission when they encounter the cluster magnetic field, as well as several background photon components. In this paper we continue to develop the MSP scenario for explaining the multi-wavelength properties of GCs by considering the entire modeling chain, including the full transport equation, refined emissivities of stellar and Galactic background photons, integration of the flux along the line of sight, and comparison with observations. As an illustration, we apply the model to Terzan 5, where we can reasonably fit both the (line-of-sight-integrated) X-ray surface flux and spectral energy density data, using the first to constrain the leptonic diffusion coefficient within the GC. We lastly discuss possible future extensions to and applications of this maturing model.

Key words: globular clusters: general – globular clusters: individual (Terzan 5) – pulsars: general – radiation mechanisms: non-thermal

Online-only material: color figures

1. INTRODUCTION

Globular clusters (GCs) are known to be ancient groups of stars held together by their mutual gravity. Given their old ages, they are expected to harbor many evolved stellar objects. In addition, their high core densities should enhance stellar encounter rates, also facilitating the formation of stellar end-products (e.g., Pooley et al. 2003). GCs do indeed contain a variety of stellar-type members, including low-mass X-ray binaries (LMXBs), thought to be the progenitors of millisecond pulsars (MSPs; Alpar et al. 1982). The abundance of LMXBs in GCs, which have been shown to correlate with the stellar encounter rate Γ_e (Gendre et al. 2003), therefore implies the presence of many GC MSPs. Given the formation history of the latter, one would expect the number of MSPs to also be related to Γ_e, similar to the number of GC LMXBs. Following this argument, Abdo et al. (2010) demonstrated a correlation between the expected number of γ-ray MSPs in GCs and Γ_e, predicting that 2600–4700 Galactic GC MSPs should be observable in γ-rays. Hui et al. (2010) have also found correlations of radio GC MSPs with Γ_e and metallicity, confirming the idea that stellar dynamical interactions are important for MSP formation, while Hui et al. (2011) could correlate MSP γ-ray luminosity (indicative of the number of MSPs in the cluster) with Γ_e and metallicity. Currently, there are roughly 160 known Galactic GCs[3] (Harris 1996; 2010 edition) moving in a spherical distribution around the Galactic center; 28 of these contain more than 144 confirmed radio pulsars,[4] the bulk of these being MSPs.

Below we summarize some relevant multi-wavelength observations of GCs and proceed to give a brief overview of GC modeling that has been done, as well as a motivation for a more advanced model, before describing recent developments of our own model.

1.1. Selected Multi-wavelength GC Observations

The *Fermi* Large Area Telescope (LAT) has now firmly established GCs as a high-energy (HE) γ-ray source class by plausibly detecting more than a dozen of them in the GeV energy band (Abdo et al. 2009, 2010; Kong et al. 2010; Tam et al. 2011; Nolan et al. 2012). The spectral properties (e.g., relatively hard spectral indices, and spectral cutoffs around a few GeV) and energetics of this radiation are consistent with cumulative emission from a population of MSPs hosted by these clusters, and on this basis, the number of MSPs ($N_{\rm MSP}$) embedded in each cluster may be estimated assuming canonical values for the average γ-ray efficiency and spin-down power (Abdo et al. 2010), albeit with large errors. *Fermi* LAT has since detected γ-ray pulsations from PSR J1823−3021A in NGC 6624 and PSR B1821−24 in M28 (Freire et al. 2011; Johnson et al. 2013; Wu et al. 2013), hinting that curvature radiation (CR) may account for at least part of the observed GeV GC emission, if not dominating in this waveband.

In the very-high-energy (VHE) domain, H.E.S.S. published upper limits on the TeV emission of 47 Tucanae (Aharonian et al. 2009) and reported the discovery of a VHE excess in the direction of Terzan 5 (Abramowski et al. 2011), but offset from the center of the GC by 4′, and having a size of $9\farcm6 \times 1\farcm8$ (compared to its tidal radius of $4\farcm6$). If truly associated with

[1] On leave from the Institut für Experimentelle und Angewandte Physik, Christian-Albrechts-Universität zu Kiel, Leibnizstrasse 11, D-24118 Kiel, Germany.
[2] This work is dedicated to the memory of Okkie de Jager, with whom many of the ideas presented here originated.
[3] http://physwww.mcmaster.ca/~harris/mwgc.dat
[4] http://www.naic.edu/~pfreire/GCpsr.html

Terzan 5, this possibly represents an inverse Compton (IC) spectral component linked with particles escaping from the MSP magnetospheres, thereby constraining the injection and transport of particles within the cluster, as well as the soft-photon energy density.

Using archival *Chandra* data, Eger et al. (2010) detected diffuse X-ray emission from Terzan 5 between its half-mass and tidal radii, peaking near the center and decreasing outward. Although a clear emission scenario could not be identified, a non-thermal one seemed to be preferable. Exploiting the larger field of view of *ROSAT*, Clapson et al. (2011) analyzed archival data in the 0.1–2.4 keV energy band and found that the diffuse X-ray emission reached the level of the Galactic diffuse component around 2.′5, with no emission being visible beyond this radius. Eger & Domainko (2012) performed a follow-up study, searching for diffuse X-ray emission from several *Fermi* LAT detected GCs, but failed to distinguish any such emission above the Galactic background. This places some constraints (e.g., $N_{\rm MSP}$ and the typical cluster magnetic field strength) on a scenario involving synchrotron radiation (SR) by particles escaping from the MSP members.

Clapson et al. (2011) measured several radio structures in the direction of Terzan 5 at 11 cm and 21 cm, but the flux was rather uncertain, and no spectral index could be inferred. There was one radio source in particular that extended from the cluster to the northwest (roughly perpendicular to the Galactic plane). Clapson et al. (2011) speculated that this emission could be the result of SR by electrons escaping from the large population of MSPs in this GC. If it is possible to show that the radio emission is firmly associated with Terzan 5, such observations could in principle limit the minimum energy of particles escaping from the MSPs.

In addition to the above observations, there have also been updated measurements of Terzan 5's distance ($d = 5.9 \pm 0.5$ kpc; Valenti et al. 2007; Ferraro et al. 2009), core radius ($R_{\rm c} = 0.'15$), half-mass radius ($R_{\rm h} = 0.'52$), tidal radius ($R_{\rm t} = 4.'6$), and total luminosity ($L_{\rm tot} \sim 8 \times 10^5\, L_\odot$; Lanzoni et al. 2011), which impacts the stellar soft-photon field, transport, and emission calculations.

1.2. Earlier GC Modeling

Harding et al. (2005) were probably the first to estimate the total contribution from GC MSPs in the GeV band by summing up individual predicted pulsed CR spectra from such an ensemble (assuming some generic pulsar beaming properties). Bednarek & Sitarek (2007) next considered the scenario where the MSPs accelerate leptons either at the shocks originating during collisions of the respective pulsar winds (characterized by a power-law particle injection spectrum) or inside the pulsar magnetospheres (assuming mono-energetic injection spectra), and while diffusing outward, Comptonizing stellar and cosmic microwave background (CMB) radiation. They predicted point-like sources of GeV and TeV emission.

Venter & de Jager (2008a) calculated pulsed CR from 100 GC MSPs by randomizing over geometry as well as period P and period time derivative $\dot{P}$. They assumed a pair-starved polar cap (PSPC) electric field (Harding et al. 2005). This HE flux scales with $N_{\rm MSP}$ (e.g., Venter & de Jager 2005) and could in principle be used to constrain the average accelerating electric field and polar cap current. Venter et al. (2010) refined this procedure, and the resulting prediction (Venter et al. 2009a) published prior to the *Fermi* detection of 47 Tucanae (Abdo et al. 2009) matched the measured spectrum within a factor of two in both energy and flux.

Cheng et al. (2010) invoked an alternative scenario to produce GeV emission and calculated IC radiation from electrons and positrons (having delta-like spectra) upscattering the CMB, stellar photons, and the Galactic background (infrared and optical). They assumed a two-valued step-like spatial dependence for their diffusion coefficient and constrained this coefficient using spatial γ-ray information from *Fermi* LAT. (Büsching et al. (2011) similarly attempted to constrain the diffusion coefficient by performing a line-of-sight (LOS) calculation to model Terzan 5's diffuse X-ray data.) Cheng et al. (2010) noted that IC emission should extend beyond 10 pc from the GC center, in principle giving rise to extended sources (depending on the resolution of the telescope). In some cases, their model also predicts VHE components. Following this idea, Hui et al. (2011) found correlations between the GeV γ-ray luminosity L_γ and the stellar encounter rate $\Gamma_{\rm e}$, as well as between L_γ and the metallicity [Fe/H]. They furthermore found correlations between L_γ and the Galactic background soft-photon energy densities in different wavebands, strengthening the case of an IC scenario for producing HE emission. On the other hand, as mentioned in Section 1.1, the powerful MSP PSR J1823−3021A supports the idea that CR also contributes to the measured GeV flux.

Venter et al. (2009a) used their CR calculation to constrain $N_{\rm MSP}$ using *Fermi* LAT data for Terzan 5 and 47 Tucanae. They performed basic particle transport assuming a steady-state scenario and Bohm diffusion, calculating IC on CMB and stellar photons using a two-zone model and an approximation of the stellar energy density profile $u(r_{\rm s})$ (see Zajczyk et al. 2013, for a similar calculation). Following Venter & de Jager (2008b), they also performed an SR calculation assuming a homogeneous cluster magnetic field B. Using *Fermi* LAT and H.E.S.S. sensitivities, they could derive constraints on $N_{\rm MSP}$ and B. The H.E.S.S. data on Terzan 5, however, imply that reacceleration of particles may take place in the GC, since they measure a power-law spectrum in the TeV band, implying a power-law particle injection spectrum. A regime where particles are solely accelerated by a PSPC electric field may therefore not be applicable (Venter et al. 2011), as the PSPC regime implies spectral shapes for the injection spectrum that deviate from power laws, with particles being accumulated around a few TeV, resulting in a bump-like structure at the highest energies (see Figure 1 of Büsching et al. 2008). The use of the PSPC field is also called into question by recent light-curve modeling of *Fermi* MSPs (Venter et al. 2009b), where the bulk of MSP light curves are best fit by outer-magnetospheric models. Prinsloo et al. (2013) extended this model by calculating $u(r_{\rm s})$ from first principles, being able to reproduce the result of Bednarek & Sitarek (2007), and noted that an outer zone should be added, as the emission does not drop off within the first two zones.

Bednarek (2012) discussed the contribution of non-accreting white dwarfs (WDs) to the γ-ray emission from GCs. Very similar, and indeed complementary, to the MSP scenario, relativistic leptons leave the magnetospheres of the WDs, upscattering the surrounding soft photons to GeV/TeV energies. While the typical spin-down luminosities of WDs are lower than those of MSPs by a factor of ∼1000, this source class may be much more numerous, outnumbering the MSPs by roughly the same factor. They may therefore inject relativistic particles containing roughly the same total power. Incorporating decay of the WD magnetic fields and different scenarios for WD formation and evolution, Bednarek (2012) concluded that,

depending on model parameters, if a few thousand WDs formed within the GC lifetime, they may produce γ-ray emission on a level detectable by the Cerenkov Telescope Array.

For a recent review of the above leptonic GC models we refer the reader to Bednarek (2011). In contrast to the leptonic models, Domainko (2011) investigated a model invoking γ-ray burst remnants as potential sources of energetic leptons and hadrons. When considering a short burst resulting from the merger of two compact stars (which are plentiful in GCs, given the high stellar densities in GC cores), a fraction of the shock wave energy may be converted to accelerate hadrons, following the explosion. Collisions of such energetic hadronic cosmic rays with ambient target nuclei may lead to subsequent π^0 decays into γ-rays. The observed VHE flux from Terzan 5 implies a total hadron energy of $\sim 10^{51}$ erg, which may plausibly be supplied by such a burst. Using the observed VHE extension of the source in the direction of Terzan 5 and comparing the burst age with typical short burst rates, Domainko (2011) noted that these numbers would be compatible for a relatively slow diffusion of hadrons within the cluster. Lastly, there may be a number of multi-wavelength signatures that may provide support for this scenario, including diffuse X-rays resulting from IC by primary electrons accelerated by the blast wave, diffuse thermal X-rays created from hot plasma heated by subrelativistic merger ejecta, and high-ionization lines.

1.3. Challenges Necessitating a Refined Modeling Approach

While the leptonic models have had some success in reproducing the (γ-ray) GC spectra, there remain several challenges, both theoretical and observational. For example, the relative contribution of IC versus CR to the GeV band is unclear (Cheng et al. 2010). The GeV spectral cutoffs of Venter et al. (2009a) are somewhat high (still using the PSPC magnetospheric model), reflecting the uncertainty in the magnetospheric acceleration potential. Some GCs have quite large measured cutoffs, which may either point to an IC origin of such emission (Tam et al. 2011), reflect uncertainties in the diffuse background, or stem from other nearby contaminating sources, which inhibit unambiguous fitting of a spectral cutoff. Also, there are large errors on the inferred $N_{\rm MSP}$ (see Table 4 of Abdo et al. 2010), impacting on the normalization of the injection spectrum. The fact that many LAT-detected GCs do not exhibit detectable levels of diffuse X-ray emission challenges the SR interpretation, or strongly constrains the cluster magnetic fields (Eger & Domainko 2012). Interestingly, while some GCs have been detected in γ-rays, no radio or X-ray MSPs have been found in their direction, raising questions about, e.g., beaming, intrinsic radio faintness, or instrumental sensitivity. The detailed acceleration of injected particles is furthermore unknown, making the actual spectral shapes of the injected particles somewhat uncertain (although this may be constrained by the measured photon spectra). The question of other sources contributing to the electromagnetic output of the GC is also intriguing.

In the case of Terzan 5, there are a few observational facts that remain to be explained. First, the VHE source is highly asymmetric and extended, and significantly offset from the GC center, while the diffuse X-ray emission is more localized and centered on the cluster. This implies (see, e.g., Cheng et al. 2010; Büsching et al. 2011; Tam et al. 2011) consideration of effects such as MSPs being born near the tidal radius, a small subpopulation of powerful MSPs possibly skewing spatial properties of the γ-ray emission, non-uniform soft energy density profiles, other contributions to $u(r_s)$, an asymmetric diffusion coefficient, proper motion of the GC, the contribution of non-MSP sources, or even background (see-through) sources. The hard index of the observed diffuse X-ray emission is also difficult to match using SR (see Section 4), raising the question of alternative interpretations for this component. Furthermore, the mismatch of the X-ray and γ-ray source shapes and extensions questions whether they have a common origin with respect to the underlying leptonic population.

In an attempt to address some of the issues mentioned above, we present a refined GC model in this paper, where we exploit the power of using both a multi-wavelength and a population approach in which we average over several single-MSP properties to minimize uncertainties. This work represents a formalization of many of our previous modeling developments. Our model now includes the following features: (1) a power-law injection spectrum; (2) an LOS calculation of the X-ray surface brightness to constrain the diffusion coefficient; (3) inclusion of a Galactic background soft-photon target energy density; (4) a refined stellar soft-photon energy density profile $u(r_{\rm s})$; and (5) full particle transport, taking into account so far diffusion and radiation losses with the assumption of spherical symmetry and a steady-state regime.

The rest of the paper is structured as follows. In Section 2, we discuss the transport equation we solve to obtain the steady-state electron spectrum (Section 2.1), the assumed particle injection spectrum (Section 2.2), the radiation loss terms (Section 2.3), soft-photon target fields (Section 2.4), and spectral emission calculations (Section 2.5). We also describe our LOS integration procedure used to find the optimal diffusion coefficient (Section 2.6). Our results (Section 3) include a brief discussion of how we inferred the diffusion coefficient (Section 3.1), the solution of the steady-state electron spectrum (Section 3.2), as well as the energy loss timescales to show in which regions radiation dominates, and where particle escape dominates (Section 3.3), as this has important consequences for the source extension. We proceed to describe our fits to the spectral energy density (SED) of Terzan 5 (Section 3.4) and offer our conclusions and outlook in Section 4.

2. THE MODEL

2.1. Transport Equation

The transport of charged energetic particles, here electrons and possibly positrons, in phase space (space and momentum) can be prescribed by a Fokker–Planck-type equation such as the Parker equation (Parker 1965) that includes diffusion (spatial and momentum), convection, sources, and linear losses (see, e.g., Kopp et al. (2012) for a more general discussion of this type of equation). If spatial convection can be neglected (see Vorster et al. 2013 for the inclusion of the latter in an application to pulsar wind nebulae), we obtain

$$\frac{\partial n_{\rm e}}{\partial t} = \boldsymbol{\nabla} \cdot (\mathcal{K} \cdot \boldsymbol{\nabla} n_{\rm e}) - \frac{\partial}{\partial E_{\rm e}}(\dot{E} n_{\rm e}) + Q, \qquad (1)$$

with $n_{\rm e}$ being the electron density, which is a function of the radius vector $\boldsymbol{r}_{\rm s}$ (pointing away from the center of the GC) and the electron energy $E_{\rm e}$, which is used here instead of the magnitude of the momentum (see Kopp et al. 2012). Here, $\mathcal{K}$ denotes the diffusion tensor, $\dot{E}$ energy losses (see Section 2.3), and Q the source term (see Section 2.2). In a first, simplified approach we assume stationarity ($\partial/\partial t = 0$), spherical symmetry, i.e., $n_{\rm e}$ depends only on the distance

$r_s = |\boldsymbol{r}_s|$ from the GC center, and scalar diffusion with diffusion coefficient κ, so that Equation (1) reduces to

$$0 = \frac{1}{{r_s}^2}\frac{\partial}{\partial r_s}\left({r_s}^2\kappa\frac{\partial n_e}{\partial r_s}\right) - \frac{\partial}{\partial E_e}(\dot{E}n_e) + Q. \quad (2)$$

This may be rewritten in the form

$$\frac{\partial n_e}{\partial E_e} = \frac{1}{\dot{E}}\left(\frac{1}{{r_s}^2}\frac{\partial}{\partial r_s}\left({r_s}^2\kappa\frac{\partial n_e}{\partial r_s}\right) - n_e\frac{\partial \dot{E}}{\partial E_e} + Q\right) \quad (3)$$

so that it can be solved numerically using a Crank–Nicolson algorithm, with ∂E_e playing the role of the time, and using a logarithmic grid in both radius and energy.

We assume a typical source term being located at $\boldsymbol{r}_s = \boldsymbol{r}_C$ that is of the form

$$Q = Q_0\frac{\delta(\boldsymbol{r}_s - \boldsymbol{r}_C)}{{E_e}^\Gamma}, \quad (4)$$

with Γ being the spectral index. Making use of Gauss's theorem, the source term can be replaced by the following boundary condition:

$$\left.\frac{\partial n_e}{\partial r_s}\right|_{r_{s,min}} = -\frac{Q_0}{4\pi {r_{s,min}}^2\kappa(E_e, r_{s,min}){E_e}^\Gamma}, \quad (5)$$

where r_{min}, bounding the spherical region containing all particle sources, is the inner boundary of our simulation region. For all results shown below we used $r_{min} = 0.01$ pc. The outer boundary was chosen as large as $r_{max} = 150$ pc $\gg R_t$ in order to justify homogeneous Dirichlet boundary conditions. The integration starts with homogeneous "initial" conditions $n_e(r_s, E_{e,max}) = 0$ at the maximum electron energy and is then performed down in energy.

In this work, we consider two different diffusion coefficients: Bohm diffusion, i.e., a diffusion depending on the magnetic field strength B,

$$\kappa(r_s, E_e) = \kappa_B\frac{E_e}{B(r_s)}, \quad (6)$$

with $\kappa_B = c/3e$, where c and e denote speed of light and the elementary charge, respectively; and a diffusion coefficient, hereafter referred to as "energy-dependent," with a power law in the electron energy of the form

$$\kappa(r_s, E_e) = \kappa_0(r_s)\left(\frac{E_e}{E_{e,0}}\right)^\alpha, \quad (7)$$

with $E_{e,0} = 1$ TeV and $\alpha = 0.6$ (see Büsching et al. 2011). For simplicity, we restrict ourselves here to spatially constant κ_0 and B.

2.2. Particle Injection Spectrum

Previously (Venter & de Jager 2008b; Venter et al. 2009a, 2011), we used results from a code that simulates the acceleration of particles in the pulsar magnetospheres using the PSPC electric field, similar to what has been done by Zajczyk et al. (2013). This approach gives an estimate for the conversion efficiency of spin-down luminosity to particle power of $\eta \sim 1\%$–2.5% (Venter & de Jager 2005) from first principles, but neglects the effect of reacceleration of particles. However, motivated by fact that H.E.S.S. detected a power-law spectrum for the VHE source that seems to be associated with Terzan 5, we now assume that the particle injection spectrum is also a power law $Q(E_e) = Q_0{E_e}^{-\Gamma}$ (see Equation (4)) with units of $\mathrm{erg}^{-1}\mathrm{s}^{-1}$, between energies $E_{e,min}$ and $E_{e,max}$. One may further argue for this spectral shape by noting that particles are plausibly accelerated in shocks formed by the collision of pulsar winds within the GC (Bednarek & Sitarek 2007). If this is the case, and the process is a stochastic Fermi-type (diffusive shock acceleration) process, a power-law shape follows naturally; see, e.g., Longair (2011) and references therein. The injection spectrum is normalized by requiring

$$\int_{E_{e,min}}^{E_{e,max}} E_e Q\, dE_e = N_{MSP}\eta\langle\dot{E}\rangle. \quad (8)$$

We can use this condition to constrain the source properties N_{MSP}, η, and the ensemble average $\langle\dot{E}\rangle$ (see Section 3.4).

2.3. Radiation Losses

From Equation (1), we see that one needs to specify $\dot{E}$, which we do below for the cases of IC scattering and SR. In the following ε is the energy of the soft-photon background, while E_γ denotes the energy of the upscattered photons. In the general case (including Thompson and Klein–Nishina limits; Blumenthal & Gould 1970) the IC loss rate is given by

$$\dot{E}_{IC}(E_e, r_s, T) = -\sum_{j=0}^{k-1}\int \chi(E_\gamma, E_e, u_{rad,j}, T_j)\frac{1}{h}dE_\gamma, \quad (9)$$

with k being the number of (blackbody) soft-photon components, T_j the photon temperature of component j, T the set of all temperatures, $u_{rad,j}$ the photon energy density, and h Planck's constant. The different soft-photon background components j are discussed in Section 2.4. The function χ is

$$\chi(E_\gamma, E_e, u_{rad,j}, T_j) = \int n_{\varepsilon,j}(r_s, \varepsilon, T_j)h\frac{E_\gamma}{E_0}\zeta(E_e, E_\gamma, \varepsilon)d\varepsilon, \quad (10)$$

with the electron rest energy $E_0 = m_{e,0}c^2$ (where $m_{e,0}$ is the electron rest mass). The collision rate ζ reads

$$\zeta(E_e, E_\gamma, \varepsilon) = \zeta_0\hat{\zeta}(E_e, E_\gamma, \varepsilon), \quad (11)$$

with the factor $\zeta_0 = 2\pi e^4 E_0 c/\varepsilon {E_e}^2$ and the function $\hat{\zeta}$ being split into four cases that depend on E_γ (see Jones 1968):

$$\hat{\zeta}(E_e, E_\gamma, \varepsilon) = \begin{cases} 0 & \text{if} \quad E_\gamma \leqslant \frac{\varepsilon {E_0}^2}{4{E_e}^2}, \\ \frac{E_\gamma}{\varepsilon} - \frac{{E_0}^2}{4{E_e}^2} & \text{if} \quad \frac{\varepsilon {E_0}^2}{4{E_e}^2} \leqslant E_\gamma \leqslant \varepsilon, \\ f(q, g_0) & \text{if} \quad \varepsilon \leqslant E_\gamma \leqslant \frac{4\varepsilon {E_e}^2}{{E_0}^2 + 4\varepsilon E_e}, \\ 0 & \text{if} \quad E_\gamma \geqslant \frac{4\varepsilon {E_e}^2}{{E_0}^2 + 4\varepsilon E_e}. \end{cases} \quad (12)$$

The function $f(q, g_0)$ occurring in the third case is

$$f(q, g_0) = 2q\ln q + (1-q)(1 + (2+g_0)q), \quad (13)$$

with $q = {E_0}^2 E_\gamma/(4\varepsilon E_e(E_e - E_\gamma))$ and $g_0(\varepsilon, E_\gamma) = 2\varepsilon E_\gamma/{E_0}^2$. With these expressions inserted into Equation (9) we finally arrive at

$$\dot{E}_{IC}(E_e, r_s, T) = -\frac{g_{IC}}{{E_e}^2}\sum_{j=0}^{k-1}\int\int n_{\varepsilon,j}(r_s, \varepsilon, T_j) \times \frac{E_\gamma}{\varepsilon}\hat{\zeta}(E_e, E_\gamma, \varepsilon)d\varepsilon dE_\gamma, \quad (14)$$

where

$$g_{\rm IC} = 2\pi e^4 c. \quad (15)$$

In the case of SR, the loss rate (averaged over all pitch angles) is given by (Blumenthal & Gould 1970)

$$\dot{E}_{\rm SR}(E_{\rm e}, r_{\rm s}) = -g_{\rm SR} {E_{\rm e}}^2 U_{\rm mag}(r_{\rm s}) = -\frac{g_{\rm SR}}{8\pi} {E_{\rm e}}^2 B^2(r_{\rm s}), \quad (16)$$

with the constant (where $\sigma_{\rm T}$ denotes the Thomson cross section)

$$g_{\rm SR} = \frac{4}{3}\frac{\sigma_{\rm T} c}{{E_0}^2} = \frac{32\pi}{9}\left(\frac{e}{E_0}\right)^4 c. \quad (17)$$

2.4. Target Soft-photon Energy Densities

To calculate $\dot{E}_{\rm IC}$, we need to specify the soft-photon densities. For a blackbody we have a photon density (e.g., Zhang et al. 2008)

$$n_{\varepsilon,{\rm j}}(r_{\rm s}, \varepsilon, T_j) = \frac{15 u_{{\rm rad},j}(r_{\rm s}, T_j)}{(\pi k_{\rm B} T_j)^4} \frac{\varepsilon^2}{e^{\frac{\varepsilon}{k_{\rm B} T_j}} - 1}, \quad (18)$$

where $u_{{\rm rad},j}$ (see Equation (9)) is the energy density of photon radiation field component j and $k_{\rm B}$ is Boltzmann's constant.

We consider the following components or sources for soft photons: CMB with $T_0 = 2.76$ K and $u_{{\rm rad},0} = 0.27$ eV cm^{-3} ($j = 0$), stellar photons with a temperature[5] of $T_1 = 4500$ K and $u_{{\rm rad},1} = u(r_{\rm s})$ ($j = 1$), and the Galactic background radiation field at the position of the GC ($j = 2$). Inserting $u_{{\rm rad},j}$, we obtain

$$n_{\varepsilon,0}(r_{\rm s}, \varepsilon, T_0) = \frac{8\pi}{h^3 c^3} \frac{\varepsilon^2}{e^{\frac{\varepsilon}{k_{\rm B} T_0}} - 1}, \quad (19a)$$

$$n_{\varepsilon,1}(r_{\rm s}, \varepsilon, T_1) = \frac{8\pi}{h^3 c^3} \frac{\varepsilon^2}{e^{\frac{\varepsilon}{k_{\rm B} T_1}} - 1} \left(\frac{1}{2}\frac{N_{\rm tot} {R_\star}^2}{{R_{\rm c}}^2 \tilde{R}}\right) \int_{r'=0}^{r'=R_{\rm t}} \hat{\rho}(r') \times \frac{r'}{r_{\rm s}} \ln\left(\frac{|r' + r_{\rm s}|}{|r' - r_{\rm s}|}\right) dr', \quad (19b)$$

while $n_{\varepsilon,2}(r_{\rm s}, \varepsilon, T_2)$ is taken from Figure 1 of Cheng et al. (2010) for Terzan 5. Note that component ($j = 0$) is already included in component ($j = 2$), so that we do not consider it separately. In component ($j = 1$), $N_{\rm tot} = M_{\rm tot}/\bar{m}$ denotes the total number of cluster stars, where $M_{\rm tot}$ is the total cluster mass and $\bar{m}$ the average stellar mass; $R_{\rm c}$ indicates the core radius, $R_{\rm h}$ the half-mass radius, $R_{\rm t}$ the tidal radius, $\tilde{R} = 2R_{\rm h} - (2/3)R_{\rm c} - {R_{\rm h}}^2/R_{\rm t}$, and $R_\star$ the average stellar radius. The normalized stellar density function is assumed to be (Bednarek & Sitarek 2007, and references therein)

$$\hat{\rho}(r') = \begin{cases} 1 & \text{if} \quad r' < R_{\rm c} \\ \left(\frac{R_{\rm c}}{r'}\right)^2 & \text{if} \quad R_{\rm c} \leqslant r' < R_{\rm h} \\ \left(\frac{R_{\rm c} R_{\rm h}}{r'^2}\right)^2 & \text{if} \quad R_{\rm h} \leqslant r' < R_{\rm t} \\ 0 & \text{if} \quad r' \geqslant R_{\rm t}. \end{cases} \quad (20)$$

For details and the derivation of Equation (19b), we refer the reader to Prinsloo et al. (2013).

2.5. Calculation of Photon Spectra

For the emissivities we use the following expressions (e.g., Zhang et al. 2008): for IC scattering

$$X_{\rm IC}(E_\gamma, r_{\rm s}) = \left(\frac{dN_\gamma}{dE_\gamma}\right)_{IC} = \frac{g_{\rm IC}}{A} \sum_{\rm j=0}^{k-1} \int\int n_{\varepsilon,{\rm j}}(r_{\rm s}, \varepsilon, T_j) \times \frac{\mathcal{N}_{\rm e}(E_{\rm e}, r_{\rm s})}{\varepsilon {E_{\rm e}}^2} \hat{\zeta}(E_{\rm e}, E_\gamma, \varepsilon) d\varepsilon dE_{\rm e}, \quad (21)$$

where $A = 4\pi d^2$ with d being the distance from the source. The quantity $\mathcal{N}_{\rm e} = \int_{\rm Shell} n_e d^3 r \approx n_{\rm e} V_{\rm Shell}$ is the number of electrons per energy in a spherical shell around $r_{\rm s}$. For all three energies ($E_{\rm e}$, ε, and E_γ) we use logarithmic grids; the integration is performed according to Venter et al. (2010).

In the case of SR

$$X_{\rm SR}(E_\gamma, r_{\rm s}) = \frac{1}{A}\frac{1}{hE_\gamma}\frac{\sqrt{3} e^3 B(r_{\rm s})}{E_0} \int\int_0^{\pi/2} \mathcal{N}_{\rm e}(E_{\rm e}, r_{\rm s}) \times \tilde{\kappa}\left(\frac{\nu}{\nu_{\rm cr}(E_{\rm e}, \vartheta, r_{\rm s})}\right) \sin^2\vartheta \, d\vartheta dE_{\rm e}, \quad (22)$$

where $\nu_{\rm cr}$ stands for the critical frequency (with pitch angle ϑ)

$$\nu_{\rm cr}(E_{\rm e}, \vartheta, r_{\rm s}) = \frac{3ec}{4\pi {E_0}^3} {E_{\rm e}}^2 B(r_{\rm s}) \sin\vartheta. \quad (23)$$

The function $\tilde{\kappa}$ (where $K_{5/3}(y)$ is a modified Bessel function of order 5/3) is

$$\tilde{\kappa}(x) = x \int_x^\infty K_{5/3}(y) dy \quad (24)$$

and is computed with the algorithm given by MacLeod (2000).

2.6. Calculation of the Skymap: LOS Integration

In order to calculate a projected skymap of radiation from the GC, we define the longitude l, with $-\pi/2 \leqslant l_{\rm min} \leqslant l \leqslant l_{\rm max} \leqslant \pi/2$ and step size Δl together with the latitude b, with $-\pi/2 \leqslant b_{\rm min} \leqslant b \leqslant b_{\rm max} \leqslant \pi/2$ and step size Δb. The distance from the observer to a point within the GC ($r_{\rm s,min} \leqslant r_{\rm s} \leqslant r_{\rm s,max}$) along the LOS at a given l and b is denoted by r with $r_{\rm min} \leqslant r \leqslant r_{\rm max}$. The LOS is divided into $n_{\rm r}$ steps of length $\Delta r = (r_{\rm max} - r_{\rm min})/(n_{\rm r} - 1)$, resulting in cells with volume V and solid angle Ω. Figure 1 illustrates the geometry assumed for the LOS procedure and the quantities introduced here; in addition, the tidal radius $R_{\rm t}$ is shown.

In a Cartesian coordinate system, with the observer being at the origin, the cluster center is located at $\boldsymbol{d} = (d, 0, 0)$, while the observed point, expressed in spherical variables, is

[5] Ferraro et al. (2009) reported the discovery of two stellar populations with different iron content and ages in Terzan 5, detected as two well-defined clumps on the red horizontal branch of a color–magnitude diagram. The brighter population is more confined to the center, younger (~6 Gyr), and more metal-rich but less numerous (~500 members) than the fainter one (with ~800 members and ages of ~12 Gyr). From spectral modeling, they obtained best-fit temperatures of $T_1 = 4500$ K for the brighter stars and $T_1 = 5000$ K for the fainter ones. For definiteness, we adopt a value of $T_1 = 4500$ K for all stars in the GC. Bednarek & Sitarek (2007) have adopted a surface temperature of 6000 K, which is the value for the Sun. Given the age of the GC stars, this value may in fact be somewhat lower. The effect of changing T_1 is seen from the proportionality $u_{{\rm rad},j} \propto T_j^4$. Changing from $T_1 = 4500$ K to $T_1 = 6000$ K would increase $u_{{\rm rad},j} \propto T_j^4$ by a factor of $(6000/4500)^4 \sim 3$ and would increase the IC flux by the same amount (see Equations (14) and (18)). This will then impact on source brightness, constraints derived on the injection source strength Q_0, and other model parameters such as $N_{\rm MSP}$, η, and $\langle \dot{E} \rangle$ from SED fitting (Section 3.4). We leave a more detailed parameter study for future work; moreover, it would be even more realistic to relax the simplifying assumption that all stars have the same properties (e.g., masses, temperatures, and radii).

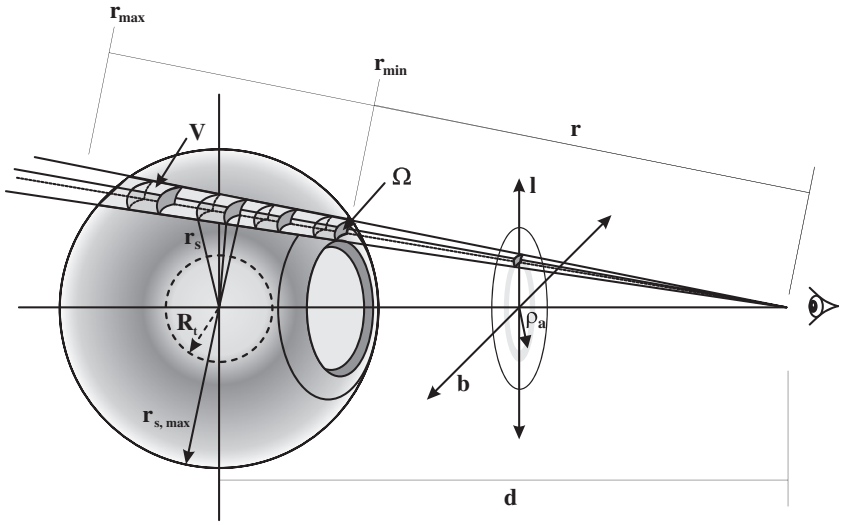

Figure 1. Illustration of the geometry for the LOS procedure; see text for details.

$\boldsymbol{r} = r(\sin\vartheta\cos\varphi, \sin\vartheta\sin\varphi, \cos\vartheta)$, where φ and ϑ are related to l and b via $l = 2\pi - \varphi = -\varphi$ and $b = \pi/2 - \vartheta$, so that $\boldsymbol{r} = r(\cos b\cos l, -\cos b\sin l, \sin b)$, and $\boldsymbol{r}_\mathrm{s} = \boldsymbol{r} - \boldsymbol{d}$ is the vector from the cluster center to the observed point, with $r_\mathrm{s}(r, l, b) = \sqrt{r^2 + d^2 - 2rd\cos l\cos b}$.

For a fixed photon energy $E_\gamma = h\nu_\gamma = hc/\lambda_\gamma$ the flux Φ is

$$\Phi(l, b, E_\gamma) = \int_{r_\mathrm{min}}^{r_\mathrm{max}} \int_{l'=l-\frac{\Delta l}{2}}^{l'=l+\frac{\Delta l}{2}} \int_{b'=b-\frac{\Delta b}{2}}^{b'=b+\frac{\Delta b}{2}} \times \frac{1}{4\pi r^2}\mathcal{X}(E_\gamma, r_\mathrm{s}(r, l', b'))\cos b'\, db' dl' r^2 dr, \quad (25)$$

where (see Equations (21) and (22))

$$\mathcal{X} = \frac{A}{V_\mathrm{shell}}(X_\mathrm{SR} + X_\mathrm{IC}). \quad (26)$$

Assuming that $\mathcal{X}$ does not vary within the cells, this can be simplified as

$$\Phi(l, b, E_\gamma) = \sum_{i=1}^{n_\mathrm{r}} \frac{V(r_i, l, b)}{4\pi {r_i}^2}\mathcal{X}(E_\gamma, r_\mathrm{s}(r_i, l, b)), \quad (27)$$

with volume element $V(r_i, l, b)$ and solid angle $\Omega(l, b)$ (see Figure 1), which are related to each other via the relation

$$V(r_i, l, b) = \frac{1}{3}\left(\left(r_i + \frac{\Delta r}{2}\right)^3 - \left(r_i - \frac{\Delta r}{2}\right)^3\right)\Omega(l, b). \quad (28)$$

In order to convert Φ into a surface flux, we first introduce the total flux in a given annulus of the projected image, represented by the gray ring with radius ρ_a in Figure 1. We use a grid also in l and b, denote the grid points by (r_i, l_j, b_k), and write

$$\Phi_\mathrm{tot}(E_\gamma, \rho_\mathrm{a}) = \sum_{jk} \Phi_{jk}(E_\gamma)\delta_{jk}^{(a)}, \quad (29)$$

where $\delta_{jk}^{(a)} = 1$ for grid points belonging to annulus ρ_a (otherwise zero) and (see Equation (27))

$$\Phi_{jk}(E_\gamma) = \sum_{i=1}^{n_\mathrm{r}} \frac{V(r_i, l_j, b_k)}{4\pi {r_i}^2}\mathcal{X}(E_\gamma, r_s(r_i, l_j, b_k)). \quad (30)$$

The total flux Φ_tot does not depend on the number of grid points, since $\Phi_{jk}(E_\gamma)$ compensates this number via its proportionality to the solid angle element $\Delta\Omega_{jk} = \Omega(l_j, b_k)$:

$$\Phi_{jk}(E_\gamma) = \Psi_{jk}(E_\gamma)\Delta\Omega_{jk}, \quad (31)$$

i.e., for a smaller number of grid points $\Delta\Omega_{jk}$ becomes larger, while

$$\Psi_{jk}(E_\gamma) = \frac{\Phi_{jk}(E_\gamma)}{\Delta\Omega_{jk}} \quad (32)$$

is a quantity independent of the size of the grid cell. The "surface brightness" $\mathcal{B}$ is introduced here as the ratio of Φ_tot and $\Omega_\mathrm{tot}^{(a)} = \sum_{jk}\Delta\Omega_{jk}\delta_{jk}^{(a)}$:

$$\mathcal{B}(E_\gamma, \rho_\mathrm{a}) = \frac{\Phi_\mathrm{tot}(E_\gamma)}{\Omega_\mathrm{tot}^{(a)}} = \frac{\sum_{jk}\Psi_{jk}\Delta\Omega_{jk}\delta_{jk}^{(a)}}{\sum_{jk}\Delta\Omega_{jk}\delta_{jk}^{(a)}} = \sum_{jk}\Psi_{jk}w_{jk}^{(a)}, \quad (33)$$

where obviously $\sum_{jk} w_{jk}^{(a)} = 1$. We can thus view Φ_tot to be the product of $\Omega_\mathrm{tot}^{(a)}$ and Ψ being averaged over the annulus: $\Phi_\mathrm{tot}(E_\gamma, \rho_\mathrm{a}) = \Omega_\mathrm{tot}^{(a)}\langle\Psi(E_\gamma)\rangle^{(a)}$.

The surface flux $\mathcal{S}$ finally is obtained by multiplying the surface brightness $\mathcal{B}$ with E_γ and integrating the product over the photon energy

$$\mathcal{S}(\rho_\mathrm{a}) = \int_{\mathrm{E}_{\gamma,\mathrm{min}}}^{E_{\gamma,\mathrm{max}}} E_\gamma\mathcal{B}(E_\gamma, \rho_\mathrm{a})dE_\gamma. \quad (34)$$

It is the quantity $\mathcal{S}(\rho_\mathrm{a})$, given in erg/(cm^2 s deg^2), for different values of $E_{\gamma,\mathrm{min}}$ and $E_{\gamma,\mathrm{max}}$, which is compared below with observations of the diffuse X-ray flux.

3. RESULTS

3.1. Inferring the Optimal Diffusion Coefficient

One of the most crucial model parameters, influencing the particle transport and source extension and thus the radiation properties of the GC, is the assumed diffusion coefficient κ. It has been customary to assume Bohm diffusion (e.g., Bednarek & Sitarek 2007; Venter et al. 2009a), while Cheng et al. (2010) used a Heaviside function in r_s. For a fixed source strength Q_0

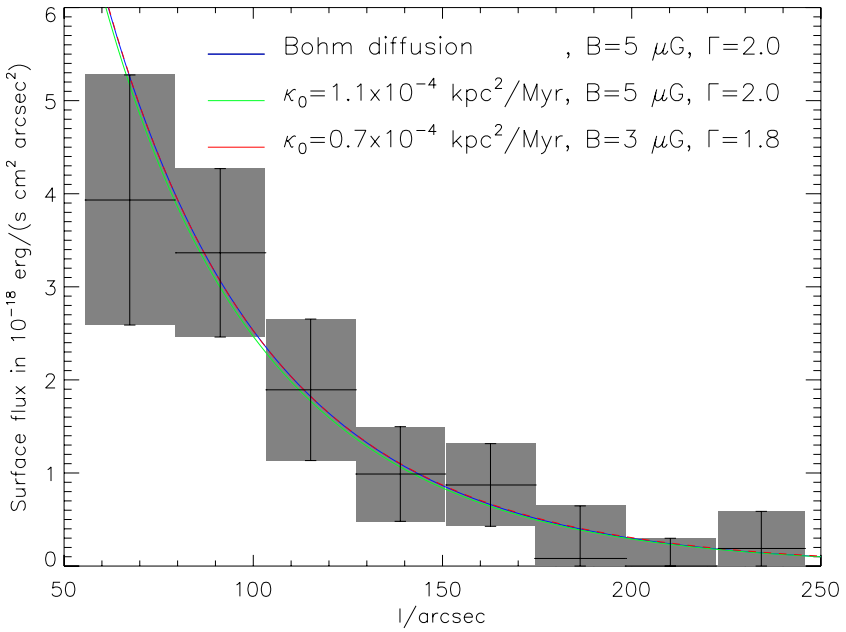

Figure 2. Diffuse X-ray profiles obtained by an LOS integration (as a function of l at $b = 0$) of the flux in the 1–7 keV band compared with measurements by the *Chandra* spacecraft (Eger et al. 2010, black crosses and gray areas). Model parameters are indicated in the legend.
(A color version of this figure is available in the online journal.)

as inferred from SED modeling (see Section 3.4 below), we infer κ using Equation (7) and performing the LOS integration described in Section 2.6. Figure 2 shows the diffuse X-ray profile measured by *Chandra* (Eger et al. 2010), as well as LOS-integrated fluxes in the 1–7 keV band obtained with our model. The blue line is for Bohm diffusion for a cluster field of $B = 4.9\,\mu$G (henceforth indicated as $5\,\mu$G), whereas the green and red lines indicate energy-dependent diffusion according to Equation (7), respectively representing $\kappa_0 = 1.1 \times 10^{-4}$ kpc^2 Myr^{-1} ($\approx 3 \times 10^{25}$ cm^2 s^{-1}), $B = 4.8\,\mu$G (henceforth indicated as $5\,\mu$G), and $\Gamma = 2.0$; and lastly $\kappa_0 = 0.7 \times 10^{-4}$ kpc^2 Myr^{-1} ($\approx 2 \times 10^{25}$ cm^2 s^{-1}), $B = 2.9\,\mu$G (henceforth indicated as $3\,\mu$G), and $\Gamma = 1.8$. While these curves are extremely close, one has to bear in mind that this is only for a very small energy range. Implications of the different diffusion coefficients will be noticeable in other energy bands (see Sections 3.3 and 3.4), so that these parameters cannot be considered as truly degenerate. For example, $\kappa_0 = 1.1 \times 10^{-4}$ kpc^2 Myr^{-1} provides a better fit to the SED, although this also depends on the choice of Γ. The choice of the diffusion coefficient will also impact on the predicted source extension (see Figure 6).

3.2. The Steady-state Electron Particle Spectrum

Figure 3 shows the steady-state particle spectrum, the numerical solution of Equation (3), as a function of electron energy E_e for different representative radii r_s, as indicated by the colored lines in the right panel, where the tidal radius R_t is shown as the black dotted line (around $\sim$10 pc). This is for the case where $\kappa_0 = 0.7 \times 10^{-4}$ kpc^2 Myr^{-1}, $B = 3\,\mu$G, and $\Gamma = 1.8$. The spectral index becomes softer than that of the injected source spectrum, increasingly so at larger distances since the particles lose energy via radiation as they diffuse through the cluster. High-energy particles are seen to lose their energy faster than the low-energy particles, as indicated by the break that develops with distance, as expected from the functional dependence (e.g., $\dot{E}_{SR} \propto E^2$) of the energy loss terms. The particle number density also decreases, particularly at high energies due to the increased

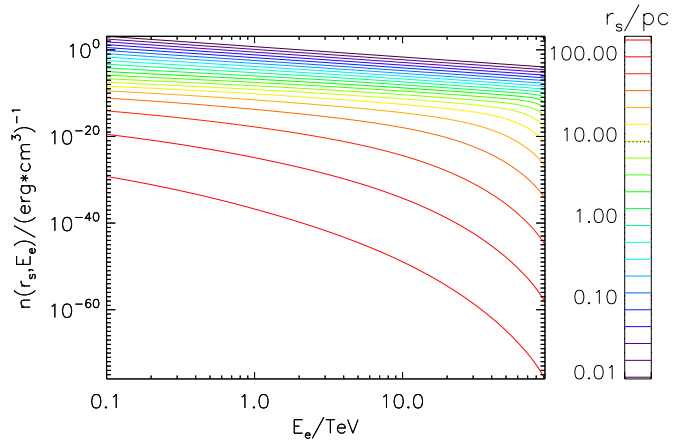

Figure 3. Steady-state particle spectrum as a function of electron energy E_e at different r_s, for $\kappa_0 = 0.7 \times 10^{-4}$ kpc^2 Myr^{-1}, $B = 3\,\mu$G, and $\Gamma = 1.8$. The colors correspond to the distance from the GC center, shown in the right panel, where the black dotted line indicates the tidal radius R_t (around $\sim$10 pc).
(A color version of this figure is available in the online journal.)

diffusion ($\kappa(E_e) \propto {E_e}^{0.6}$ or $\propto E_e$ in the Bohm case). It is interesting to note that many particles still have substantial energy at the tidal radius and continue to radiate far beyond this radius. This has implications for the source size (see Section 3.3).

3.3. Loss Timescales and Source Extension

Figure 4 shows radiative loss timescales (dashed lines) $\tau_{rad}(r_s, E_e) = E_e/\dot{E}(r_s, E_e)$, escape (diffusive loss) times (dash-dotted) $\tau_{esc} = (r_{s,+}^2 - r_{s,-}^2)/2\kappa$ with $r_{s,\pm} = r_s \pm \Delta r/2$ with the shell thickness Δr, as well as the total (effective) timescales (solid lines) $\tau_{tot} = \tau_{rad}\tau_{esc}/(\tau_{rad} + \tau_{esc})$ (e.g., Zhang et al. 2008). The color again indicates the radius, and we use the parameters $\kappa_0 = 0.7 \times 10^{-4}$ kpc^2 Myr^{-1}, $B = 3\,\mu$G, and $\Gamma = 1.8$. Particle escape by diffusion dominates at small radii, while radiation losses start to have an effect at radii close to the

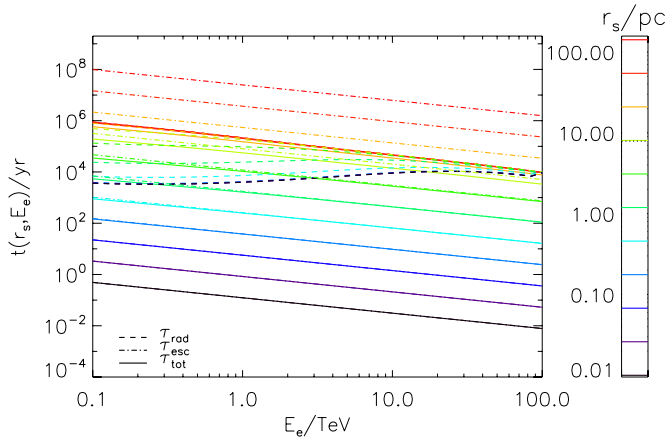

Figure 4. Loss timescales as a function of electron energy for different distances from the GC center (color). The solid lines stand for the effective loss timescales, the radiation losses are shown by the dashed lines, while escape times by diffusion are indicated by the dash-dotted lines. In this case $\kappa_0 = 0.7 \times 10^{-4}$ kpc^2 Myr^{-1}, $B = 3\,\mu$G, and $\Gamma = 1.8$.

(A color version of this figure is available in the online journal.)

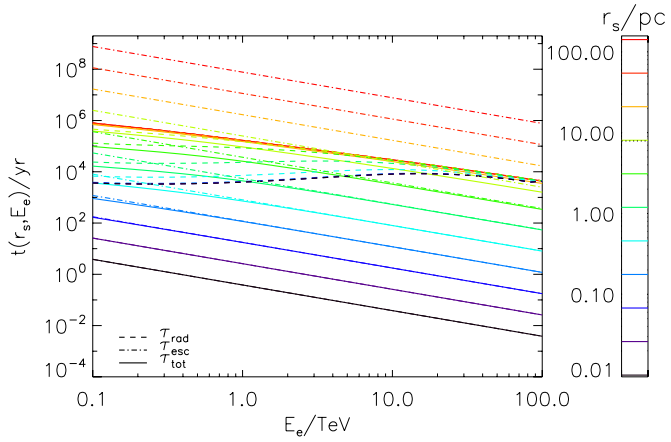

Figure 5. Same as Figure 4, but for Bohm diffusion with $B = 5\,\mu$G.

(A color version of this figure is available in the online journal.)

tidal radius, especially for smaller particle energies (since these particles take longer to escape). The effective loss timescales therefore change shape (deviating from straight lines) as this change in regime occurs when moving to larger distances. For Bohm diffusion, shown in Figure 5, the picture is quite similar, given the fact that the magnitudes of the coefficients are in the same range. The energy dependence of the escape times is now somewhat steeper ($\tau_{\rm esc} \propto {E_{\rm e}}^{-1}$ for the Bohm case, versus ${E_{\rm e}}^{-0.6}$), so that high-energy particles escape relatively faster. The effect of radiation losses (especially IC) therefore starts to become visible at relatively smaller radii in the Bohm case (see Figure 7), which leads to a slightly smaller γ-ray source extension. We furthermore note that $\tau_{\rm tot}$ is much smaller than the age of the system, so that several generations of particles are needed to ensure a steady flux; this means a continuous injection of particles over long timescales. Figure 6 shows the surface flux (see Equation (34), but with the integrand divided by E_γ) resulting from an LOS integration for the γ-ray (solid lines) and X-ray (dashed lines) sources versus the angular distance (longitude) from the GC center. Red represents the energy-dependent diffusion case with $\kappa_0 = 0.7 \times 10^{-4}$ kpc^2 Myr^{-1}, $B = 3\,\mu$G, and $\Gamma = 1.8$ (see Figure 4), while green represents Bohm diffusion (see Figure 5), using $B = 5\,\mu$G and $\Gamma = 2.0$.

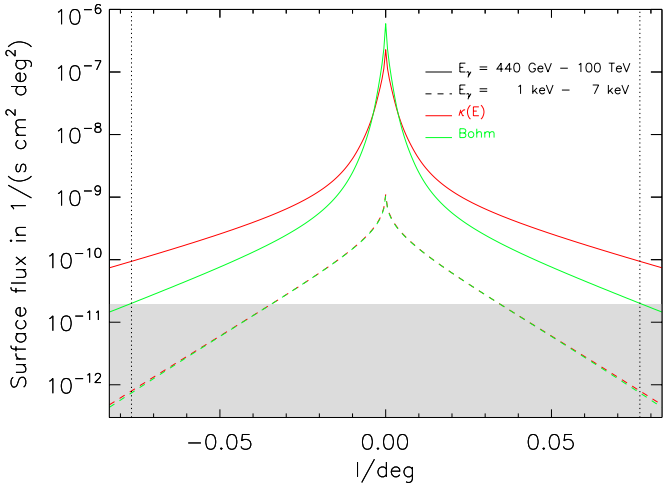

Figure 6. Surface flux (see Equation (34), but with the integrand divided by E_γ to facilitate comparison with data) for the γ-ray (solid lines) and X-ray (dashed lines) sources as a function of the angular distance (longitude) from the GC center. Red stands for the energy-dependent diffusion case ($\kappa_0 = 0.7 \times 10^{-4}$ kpc^2 Myr^{-1}, $B = 3\,\mu$G, and $\Gamma = 1.8$), while green indicates Bohm diffusion ($B = 5\,\mu$G, $\Gamma = 2.0$). The Galactic diffuse X-ray background level is shown by the gray band. The dotted vertical lines show the tidal radius.

(A color version of this figure is available in the online journal.)

It is clear that the source size depends on the assumption for the diffusion coefficient. The dotted vertical lines again indicate the tidal radius. The Galactic diffuse X-ray background level is shown by the gray band. When fitting the γ-ray source profile using a Gaussian function, one obtains a half width of $\sim 2'$–$3'$, assuming spherical symmetry. (The observed γ-ray source extension is asymmetric and was fit by a two-dimensional Gaussian with best-fit half widths of $9\farcm6$ and $1\farcm8$; Abramowski et al. 2011.) For comparison one may furthermore estimate the expected γ-ray surface brightness by dividing the measured flux by the solid angle subtended by the source (or similarly, by normalizing the 2D Gaussian using the measured flux). This leads to values of $\sim 10^{-7}$–10^{-6} s^{-1} cm^{-2} deg^{-2}, depending on the exact assumptions used, which is similar to our model predictions for the peak brightness, even though our brightness profile is non-Gaussian in shape. We note that the γ-ray surface flux is much larger than the X-ray surface flux, given the large difference in the respective energy bands over which the integral is carried out.

To illustrate the effect of choosing different diffusion coefficients further, Figure 7 shows the contour plot of $E_\gamma^2 dN_\gamma/dE_\gamma$ as a function of $r_{\rm s}$ and $E_{\rm e}$, i.e., *prior* to LOS integration. The top panel is for Bohm diffusion ($B = 5\,\mu$G and $\Gamma = 2.0$), and the bottom one for the energy-dependent diffusion (with $\kappa_0 = 0.7 \times 10^{-4}$ kpc^2 Myr^{-1}, $B = 3\,\mu$G, and $\Gamma = 1.8$). The plot shows the "bumps" corresponding to the SR (lower bump) and IC scattering (upper one) spectral components, as functions of radius and photon energy. While the SR components are similar, there is a clear distinction between the IC ones. In the Bohm case, the IC radiation generally originates at quite smaller radii (as noted above; see Figure 5), given the softer energy dependence of the coefficient, leading to a relatively smaller γ-ray source. We note that significant γ-ray emission may still occur outside the tidal radius in the energy-dependent case. There is also a shift in radius between the SR and IC peaks, particularly in the Bohm case. This property may be useful in future when modeling offset X-ray and γ-ray sources as is observed in the case of Terzan 5. However, this effect will be less

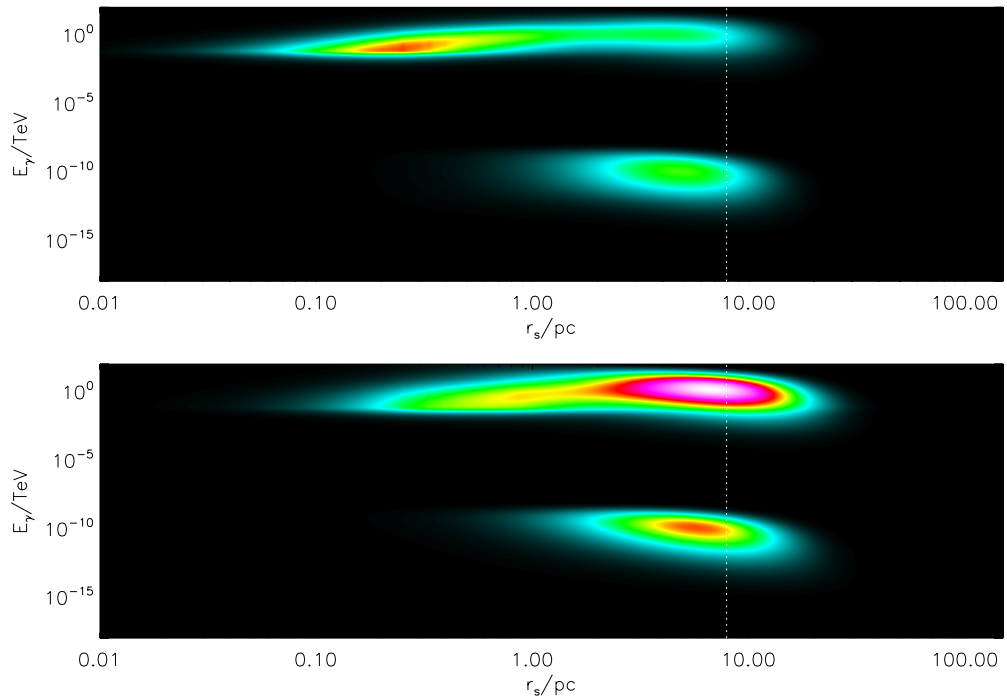

Figure 7. Contour plots of *non-LOS-integrated* $E_\gamma^2 dN_\gamma/dE_\gamma$ as a function of r_s and E_γ. The top panel is for Bohm diffusion ($B = 5\,\mu$G, $\Gamma = 2.0$), and the bottom one for energy-dependent diffusion, with $\kappa_0 = 0.7 \times 10^{-4}$ kpc^2 Myr^{-1}, $B = 3\,\mu$G, and $\Gamma = 1.8$. The white dotted lines indicate the tidal radius.
(A color version of this figure is available in the online journal.)

visible after performing the LOS integration, and we caution the reader that, because of our assumption of spherical symmetry, these bumps should be imagined as rings or annuli, rather than bump-like structures, as the latter will not show up in an LOS-integrated image. One should therefore make the distinction between the LOS-integrated "observer's view" presented in Figure 6 and the "model view" presented in Figure 7. Even in the case where the X-ray and γ-ray emission production sites are not co-located, the integrated surface brightness profiles will peak near the cluster center, which is a result of the LOS integration procedure, sampling radiation from concentric annuli centered on the GC.

Turning our attention to the IC spectral component, we investigate the integral flux:

$$\mathcal{F}(>E_{\gamma,0}) = \int_{E_{\gamma,0}}^{\infty} \frac{dN_\gamma}{dE_\gamma} dE_\gamma \qquad (35)$$

for $E_{\gamma,0} = 440$ GeV (Abramowski et al. 2011). Figure 8 shows the effect of the different soft-photon target fields. In the case where we consider stellar photons alone (black solid line, assuming $T_1 = 4500$ K) the flux peaks inside the cluster, close to the half-mass radius R_h ($\sim$0.9 pc). Outside the cluster there is still some contribution since the stellar energy density falls off as $1/r_s^2$ in this region. If we consider the CMB target photons alone (green solid line), we find, however, a peak beyond 20 pc, i.e., outside the cluster. The same applies to the Galactic background component (red solid line) giving an even higher flux, because it contains the CMB, demonstrating the non-negligible influence of the latter, and leading to an increased extension of the γ-ray source. The green-black and red-black dashed lines indicate the combination of CMB plus stellar and Galactic background plus stellar contributions, respectively. We therefore note that in addition to specifying κ, the choice of soft-photon components is also important for the predicted source extension and flux.

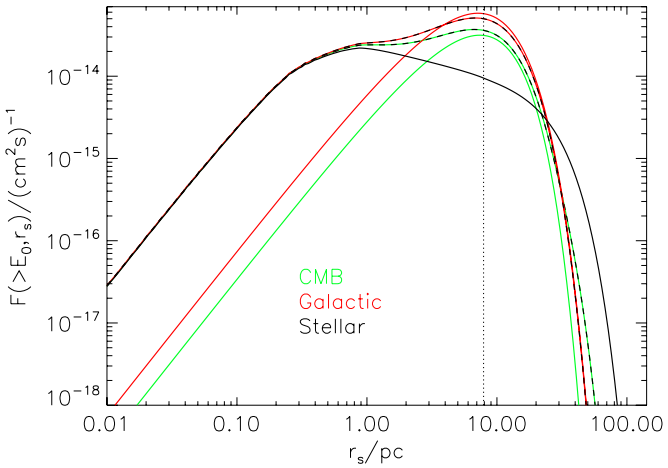

Figure 8. The *non-LOS-integrated* integral IC flux (Equation (35)) above $E_0 = 440$ GeV as a function of source radius, for the case of energy-dependent diffusion ($\kappa_0 = 0.7 \times 10^{-4}$ kpc^2 Myr^{-1}, $B = 3\,\mu$G, and $\Gamma = 1.8$), indicating the different soft-photon contributions. The black solid line stands for stellar photons only (using $T_1 = 4500$ K), the green one for CMB only, and the red one for Galactic background photons, including the CMB contribution. The dashed lines indicate contributions from two components (as indicated by the respective colors). The dotted vertical line again shows the tidal radius.
(A color version of this figure is available in the online journal.)

As noted in Section 1.3, the asymmetric shape of the Terzan 5 VHE source may be due to several reasons, e.g., an asymmetric distribution of particle sources, or non-uniform soft-photon backgrounds. One may also attempt to model such an asymmetry by invoking a spatially asymmetric diffusion coefficient. The latter may reflect turbulent, inhomogeneous properties of the cluster magnetic field. Refinements such as contemplated above are, however, beyond the scope of the current paper, since we restrict our attention to the case involving spherical symmetry. Future work should relax this restriction.

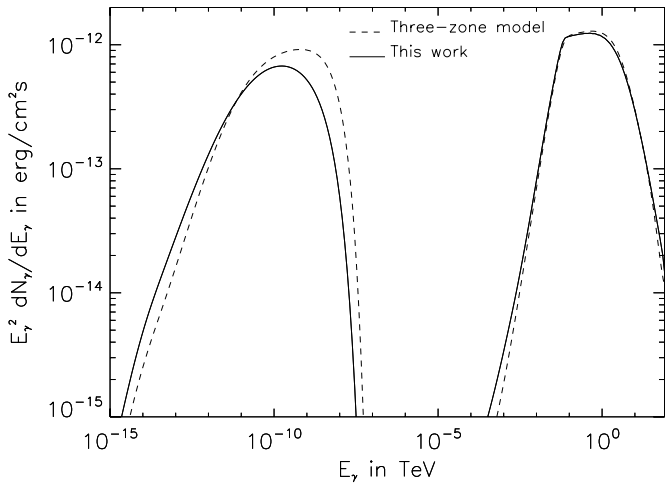

Figure 9. SED plot for Terzan 5 indicating our predicted SR and IC components, assuming Bohm diffusion, with the dashed black lines standing for the results by Prinsloo et al. (2013) for a three-zone model, and the solid black lines for the results of this work, both for a cluster field of $B = 10\,\mu$G and $T_1 = 6000$ K.

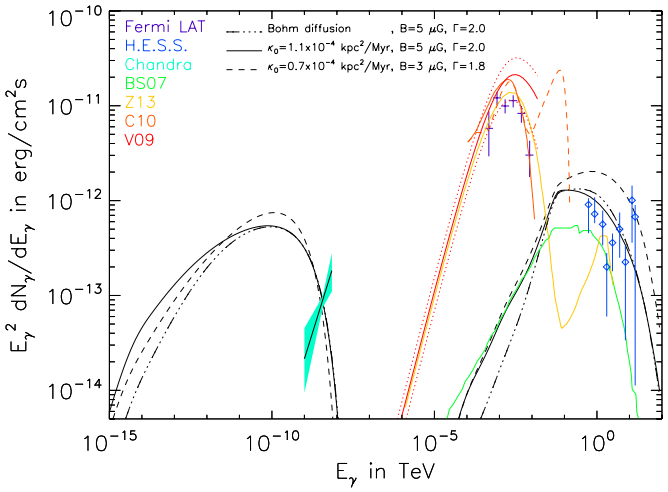

Figure 10. Same as Figure 9, but for both one Bohm and two energy-dependent diffusion coefficients (see legend for parameters). We also indicate a CR component (solid red line with dotted red lines indicating the errors) from Venter et al. (2009a, V09) from which we can infer $N_{\rm MSP}$. We also show *Chandra* data (cyan butterfly; Eger et al. 2010), *Fermi* LAT data (purple crosses; Abdo et al. 2010), and H.E.S.S. data (open blue squares; Abramowski et al. 2011). In addition, we indicate alternative IC models in the GeV range (orange solid and dashed lines; Cheng et al. 2010, C10) and TeV range (Bednarek & Sitarek 2007, BS07; green solid line) being scaled to the same model parameters we used (cluster distance and a somewhat smaller MSP spin-down luminosity) together with a recent CR plus IC model using an injection spectrum calculated in a PSPC model (Zajczyk et al. 2013, Z13; yellow solid line).

(A color version of this figure is available in the online journal.)

3.4. Fit to the SED of Terzan 5

Figure 9 shows the predicted SED components of Terzan 5 in the case of Bohm diffusion, comparing the results by Prinsloo et al. (2013) using a three-zone model (dashed black lines) with those of this work (solid black lines), both for a cluster field of $B = 10\,\mu$G. Note that Prinsloo et al. (2013) used $T_1 = 6000$ K, so that we used the same value in this plot. We observe a very good correspondence between the IC components, while there are some deviations in the SR components. The latter may reflect the difference in the particle transport approaches (three spatial zones versus a grid with 81 points) and different numerical treatment of Equation (24).

Figure 10 shows the SED for Terzan 5 in the case of the energy-dependent diffusion coefficient. The solid lines represent the case for $\kappa_0 = 1.1 \times 10^{-4}$ kpc^2 Myr^{-1}, $B = 5\,\mu$G, and $\Gamma = 2.0$, while the dashed lines represent $\kappa_0 = 0.7 \times 10^{-4}$ kpc^2 Myr^{-1}, $B = 3\,\mu$G, and $\Gamma = 1.8$. The Bohm case is represented by the dash-dotted lines. We also include multi-wavelength observations and other model results as described in the figure caption. We note that we cannot fit the diffuse radio emission (Clapson et al. 2011), given the inferred values for κ_0 using the X-ray surface brightness profile. If we were to choose larger values for κ_0, we could obtain radio spectral fits when lowering the minimum lepton energy to a few GeV. However, such large κ_0 would contradict the X-ray data. This discrepancy may call into question whether the radio emission is indeed associated with Terzan 5, or whether an alternative spectral component is needed to fit the X-ray data (see Section 4). We will consider the effects of changing the model parameters in an upcoming paper (C. Venter & A. Kopp, in preparation) and therefore do not claim that this is the optimal fit for the SED of Terzan 5; it is merely illustrative.

Concerning the X-ray data, Eger et al. (2010) found quite a hard photon index of 0.9 ± 0.5 for the diffuse X-ray emission. There might be systematic uncertainties in addition to the quoted statistical error, but these are not easy to quantify in the case of only a single observation with a single instrument. The mismatch between the measured and predicted spectral index could therefore be explored further by deeper X-ray observations of this region. The analysis method seems robust, however, since this has also been employed when analyzing diffuse spectra from several pulsar-wind nebulae, yielding photon indices in the range 1.5–2.5, depending on the distance to the pulsar, consistent with previous independent analyses (P. Eger 2012, private communication). This mismatch may also point to the need for invoking other physical processes that may result in additional spectral components (see Section 4).

The normalization of the injection spectrum (Equation (8)) gives

$$Q_0 = \begin{cases} (2-\Gamma)\dfrac{N_{\rm MSP}\eta\langle\dot{E}\rangle}{E_{\rm e,max}{}^{2-\Gamma} - E_{\rm e,min}{}^{2-\Gamma}} & \text{if} \quad \Gamma \neq 2, \\ \dfrac{N_{\rm MSP}\eta\langle\dot{E}\rangle}{\ln\left(E_{\rm e,max}/E_{\rm e,min}\right)} & \text{if} \quad \Gamma = 2. \end{cases} \tag{36}$$

Our fits (Figure 10) imply a source strength of $Q_0 \approx 6.33 \times 10^{33}$ erg^{-1} s^{-1}, therefore constraining the combination (product) of the number of MSPs $N_{\rm MSP}$, the particle conversion efficiency η, and the average MSP spin-down power $\langle\dot{E}\rangle$, depending on Γ, $E_{\rm e,max}$, and $E_{\rm e,min}$. Taking, for example, $\Gamma = 1.8$, $E_{\rm e,max} = 100$ TeV, and $E_{\rm e,min} = 0.1$ TeV, the needed source strength could be supplied by $N_{\rm MSP} \sim 34$ MSPs (the current number of radio GC MSPs detected in this cluster) with typical efficiencies of $\sim$4% and an average spin-down luminosity of 5×10^{34} erg s^{-1} (or $\eta \sim 10\%$ and $\langle\dot{E}\rangle \sim 2 \times 10^{34}$ erg s^{-1}). For the case of $\Gamma = 2.0$, one could have combinations such as $N_{\rm MSP} \sim 34$, $\eta \sim 6.4\%$, $\langle\dot{E}\rangle \sim 2 \times 10^{34}$ erg s^{-1} or $N_{\rm MSP} \sim 34$, $\eta \sim 3\%$, $\langle\dot{E}\rangle \sim 5 \times 10^{34}$ erg s^{-1}. If we set $N_{\rm MSP} \sim 60$ as inferred by Venter et al. (2011) by comparing their predicted CR spectrum with the *Fermi* measurements, we obtain $\eta\langle\dot{E}\rangle \lesssim 1.1 \times 10^{33}$ erg s^{-1} for $\Gamma = 1.8$ and $\eta\langle\dot{E}\rangle \lesssim 7.2 \times 10^{32}$ erg s^{-1} for $\Gamma = 2.0$. Note that η now includes the effect of reacceleration and should therefore be an upper limit to the actual particle conversion efficiency defined within the pulsar magnetosphere itself. (The example constraints derived in this paragraph assume that the stellar properties remain fixed, so that the stellar energy

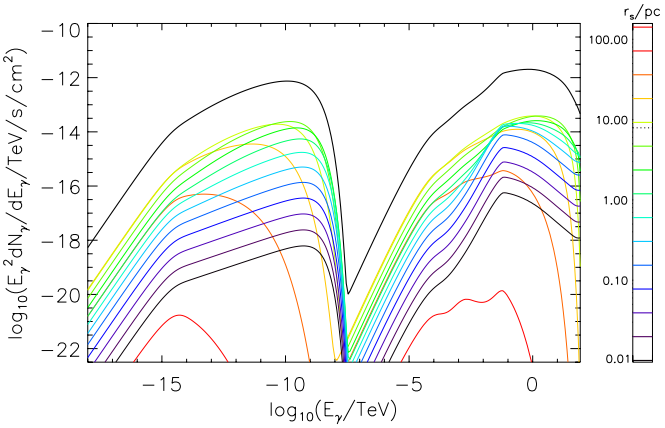

Figure 11. Spectra from different regions in the cluster for the case $\kappa_0 = 0.7 \times 10^{-4}$ kpc^2 Myr^{-1}, $B = 3\,\mu$G, and $\Gamma = 1.8$. The colors indicate representative cluster radii, indicating that a significant contribution still comes from near and beyond the tidal radius.

(A color version of this figure is available in the online journal.)

density $u(r_s) \propto N_{\rm tot} R_\star{}^2\, T_1{}^4$ does not change, leaving the IC flux unchanged.) The above parameter constraints seem quite reasonable: the value $N_{\rm MSP} = 34$ may be considered a lower limit (Hessels et al. 2006); Venter & de Jager (2005) numerically obtained $\eta \sim 1\%$–2.5% for the case of the field MSP PSR J0437−4715, using a PSPC model; and Abdo et al. (2010) adopted a value of $\langle \dot{E} \rangle \lesssim 1.8 \times 10^{34}$ erg s^{-1} when constraining the MSP population in several γ-ray GCs they observed.

In order to study the radial dependence of the cluster radiation, we plot the relative contributions from several representative r_s in Figure 11, for the case $\kappa_0 = 0.7 \times 10^{-4}$ kpc^2 Myr^{-1}, $B = 3\,\mu$G, and $\Gamma = 1.8$. We find that close to the cluster center, the emission is low, then it grows, before the contribution from the outer regions becomes lower again. This supports our findings described in Section 3.3. The thick black envelope represents the total emission from the cluster (see Figure 10).

4. DISCUSSION AND CONCLUSIONS

GCs contain many MSPs that act as strong sources of relativistic electrons. The latter may interact with the ambient magnetic and soft-photon environment, producing multi-wavelength radiation. In this case, various measurements at different wavelengths (including both spatial and spectral information) in combination with numerical simulations can be used to constrain transport, emission, and cluster parameters. Here, we present a refined model going beyond previous approaches by self-consistently following the entire model chain from the full transport equation, via the computation of the SR and IC emissivities, including stellar and Galactic background photons for the IC, to an LOS integration allowing for the comparison with observations. After benchmarking our newly developed numerical code by reproducing our previous spectral results, we are for the first time able to simultaneously fit both (LOS-integrated) X-ray surface flux data and broadband SED data for Terzan 5. From this we find that a diffusion coefficient with a power-law dependence of the electron energy can provide a reasonable LOS fit. The γ-ray source extension is somewhat larger relative to the Bohm case, since the bulk of the emission comes from near and beyond the tidal radius of Terzan 5.

We note that our predicted SR spectral shape seems to contradict the X-ray data. Apart from citing observational uncertainties that are due to the astrophysical background determination or unresolved point sources below the detection threshold, the question arises whether there exists an alternative physical solution to the origin of the diffuse X-ray emission seen in the direction of Terzan 5. While a full calculation of a new spectral component is beyond the scope of the current paper, we note that there are some recent papers that have considered the same question. Okada et al. (2007) measured extended, diffuse X-ray emission from six GCs (excluding Terzan 5). The emission was also offset from the respective cluster centers. Okada et al. (2007) grouped the detected sources into two classes. The first class is characterized by arclike morphologies and thermal spectra, interpreted as thermal emission from shock-heated plasma. The second class exhibits a clumpy structure and likely non-thermal spectra (with indices $\sim$2) and may be associated with cospatial radio sources. X-rays from these sources may originate via non-thermal bremsstrahlung, when shock-accelerated electrons interact with locally compressed gas clouds. The shock formation is thought to occur as the GC moves through the Galactic halo plasma. Eger & Domainko (2012) argued that these conditions are probably not applicable to Terzan 5. Clapson et al. (2011) noted that a non-thermal bremsstrahlung process seemed to be excluded given the lack of observational support for high-density regions (which would provide target material causing electron deflection and emission) at this source position. On the other hand, Clapson et al. (2011) argued that the diffuse X-ray data may be plausibly explained within an IC scenario (accompanied by SR radio emission), while noting that a more accurate radio index would provide further constraints. Eger & Domainko (2012) searched for significant diffuse X-ray emission from six GCs (excluding Terzan 5), but found none. They concluded that while X-rays from SR in an MSP scenario cannot be confidently rejected, an IC scenario based on the presence of a γ-ray burst remnant with the same properties as proposed for Terzan 5 (Domainko 2011) can be ruled out for all of these GCs. Eger & Domainko (2012) also mentioned that the X-ray spectrum could represent the low-energy tail of the IC component peaking at TeV energies (see Cheng et al. 2010). Another idea is that the measured spectrum may in fact be the low-energy tail of SR produced by pairs within the MSP magnetospheres, similar to what has been modeled for the Crab (Harding et al. 2008), if indeed enough energetic pairs are produced in the MSP magnetospheres. Claims for alternative spectral components should be tested by detailed future modeling of the full broadband emission.

While the current work concentrates on technical details and the development of the numerical code, there are several applications that we are now able to pursue in follow-up publications. These include modeling of the offset and asymmetrical shape of the VHE Terzan 5 source with respect to the X-ray emission (e.g., invoking an asymmetric diffusion coefficient or cluster magnetic field), a more dedicated parameter study for Terzan 5 (C. Venter & A. Kopp, in preparation), constraining the SR properties of a population of GCs using diffuse X-ray observations (Eger & Domainko 2012), and considering the effect of several other assumptions regarding the GC stellar properties on the stellar energy density profile. Recently, H.E.S.S. published an upper limit for the TeV flux of 15 GCs obtained by a stacking analysis (Abramowski et al. 2013), which is lower than predicted by a simple leptonic scaling model. It will lastly be interesting to address this discrepancy by applying our new model to this population.

We are grateful to Peter Eger, André-Claude Clapson, Michael Vorster, Johan van der Walt, and Paulus Krüger for informative discussions. This work was supported by the South African National Research Foundation (NRF).

REFERENCES

Abdo, A. A., Ackermann, M., Ajello, M., et al. 2009, Sci, 325, 845
Abdo, A. A., Ackermann, M., Ajello, M., et al. 2010, A&A, 524, 75
Abramowski, A., Acero, F., Aharonian, F., et al. 2011, A&A, 531, L18
Abramowski, A., Acero, F., Aharonian, F., et al. 2013, A&A, 551, 26
Aharonian, F., Akhperjanian, A. G., Anton, G., et al. 2009, A&A, 499, 273
Alpar, M. A., Cheng, A. F., Ruderman, M. A., & Shaham, J. 1982, Natur, 300, 728
Bednarek, W. 2011, in High-energy Emission from Pulsars and Their Systems, ed. D. F. Torres & N. Rea (Heidelberg: Springer), 85
Bednarek, W. 2012, JPhG, 39, 065001
Bednarek, W., & Sitarek, J. 2007, MNRAS, 377, 920 (BS07)
Blumenthal, G. R., & Gould, R. J. 1970, RvMP, 42, 237
Büsching, I., Venter, C., & de Jager, O. C. 2008, AdSpR, 42, 497
Büsching, I., Venter, C., Kopp, A., de Jager, O. C., & Clapson, A. C. 2011, in Proc. 32nd ICRC (Beijing)
Cheng, K. S., Chernyshov, D. O., Dogiel, V. A., Hui, C. Y., & Kong, A. K. H. 2011, ApJ, 723, 1219 (C10)
Clapson, A.-C., Domainko, W. F., Jamrozy, M., Dyrda, M., & Eger, P. 2011, A&A, 532, 47
Domainko, W. F. 2011, A&A, 533, L5
Eger, P., & Domainko, W. 2012, A&A, 540, A17
Eger, P., Domainko, W., & Clapson, A.-C. 2010, A&A, 513, A66
Ferraro, F. R., Dalessandro, E., Mucciarelli, A., et al. 2009, Natur, 462, 483
Freire, P. C. C., Abdo, A. A., Ajello, M., et al. 2011, Sci, 334, 1107
Gendre, B., Barret, D., & Webb, N. 2003, A&A, 403, L11
Harding, A. K., Stern, J. V., Dyks, J., & Frackowiak, M. 2008, ApJ, 680, 1378
Harding, A. K., Usov, V. V., & Muslimov, A. G. 2005, ApJ, 622, 531
Harris, W. E. 1996, AJ, 112, 1487
Hessels, J. W. T., Ransom, S. M., Stairs, I. H., et al. 2006, Sci, 311, 1901
Hui, C. Y., Cheng, K. S., & Taam, R. E. 2010, ApJ, 714, 1149
Hui, C. Y., Cheng, K. S., Wang, Y., et al. 2011, ApJ, 726, 100
Johnson, T. J., Guillemot, L., Kerr, M., et al. 2013, ApJ, 778, 106
Jones, F. C. 1968, PhRv, 167, 1159
Kong, A. K. H., Hui, C. Y., & Cheng, K. S. 2010, ApJ, 712, 36
Kopp, A., Büsching, I., Strauss, R. D., & Potgieter, M. S. 2012, CoPhC, 183, 530
Lanzoni, B., Ferraro, F. R., Dalessandro, E., et al. 2010, ApJ, 717, 653
Longair, M. S. 2011, High Energy Astrophysics (Cambridge: Cambridge University Press)
MacLeod, A. J. 2000, NIMPA, 443, 540
Nolan, P. L., Abdo, A. A., Ackermann, M., et al. 2012, ApJS, 199, 31
Okada, Y., Kokubun, M., Yuasa, T., & Makishima, K. 2007, PASJ, 59, 727
Parker, E. N. 1965, P&SS, 13, 9
Pooley, D., Lewin, W. H. G., Anderson, S. F., et al. 2003, ApJL, 591, L131
Prinsloo, P. L., Venter, C., Büsching, I., & Kopp, A. 2012, in Proc. SAIP, submitted (arXiv:1311.3791)
Tam, P. H. T., Kong, A. K. H., Hui, C. Y., et al. 2011, ApJ, 729, 90
Valenti, E., Ferraro, F. A., & Origlia, L. 2007, AJ, 133, 1287
Venter, C., & de Jager, O. C. 2005, ApJL, 619, L167
Venter, C., & de Jager, O. C. 2008a, ApJL, 680, L125
Venter, C., & de Jager, O. C. 2008b, in AIP Conf. Proc. 1085, High Energy Gamma-ray Astronomy, ed. F. A. Aharonian, W. Hofmann, & F. Rieger (Melville, NY: AIP), 277
Venter, C., & de Jager, O. C. 2010, ApJ, 725, 1903
Venter, C., de Jager, O. C., & Clapson, A.-C. 2009a, ApJL, 696, L52 (V09)
Venter, C., de Jager, O. C., Kopp, A., & Büsching, I. 2011, in Proc. 2011 Fermi Symp., Rome, ed. A. Morselli, eConf C110509 (arXiv:1111.1289)
Venter, C., Harding, A. K., & Guillemot, L. 2009b, ApJ, 707, 800
Vorster, M. J., Ferreira, S. E. S., de Jager, O. C., & Djannati-Ataï, A. 2013, A&A, 551, A127
Wu, J. H. K., Hui, C. Y., Wu, E. M. H., et al. 2013, ApJL, 765, L47
Zajczyk, A., Bednarek, W., & Rudak, B. 2013, MNRAS, 432, 3462 (Z13)
Zhang, L., Chen, S. B., & Fang, J. 2008, ApJ, 676, 1210